Damage Detection Sensitivity Characterization of Acousto-Ultrasound-based SHM Techniques

Vishnuvardhan Janapati[1], Fotis Kopsaftopoulos[2,*], Frank Li[1], Sang Jun Lee[1], Fu-Kuo Chang[2]

1. Acellent Technologies Inc., 835 Stewart Drive, Sunnyvale, CA 94085, USA
2. Structures and Composites Laboratory, Department of Aeronautics and Astronautics, Stanford University, CA 94305, USA

Abstract

Reliability quantification is a critical and necessary process for the evaluation and assessment of any inspection technology that may be classified either as a Nondestructive Evaluation (NDE) or Structural Health Monitoring (SHM) technique. Based on the sensitivity characterization of NDE techniques, appropriate processes have been developed and established for the reliability quantification of their performance with respect to damage/flaw detection in materials or structures. However, in the case of SHM-based methods, no such well-defined and general applicable approaches have been established for neither active nor passive sensing techniques that allow for their accurate reliability quantification.

The objective of this study is to characterize the sensitivity of active sensing acousto-ultrasound-based SHM techniques with respect to damage detection, as well as to identify the parameters that influence their sensitivity. With such an understanding, it is believed that adequate quantitative methods could then be established to enable the practical use of acousto-ultrasound SHM methods in the aerospace and mechanical engineering communities.

In order to evaluate the sensitivity of a pre-selected active sensing acousto-ultrasound SHM system, both numerical simulations and experiments were performed on thirty aluminum coupons each outfitted with a pair of Lead-Zirconate-Titanate (PZT) based piezoelectric sensors/actuators. A damage index versus damage size relationship was investigated numerically and experimentally to assess the applicability of the traditional NDE linear regression framework for Probability of Detection (POD) for an active sensing SHM system. The results of the study show that the position of each sensor-actuator pair with respect to a known damage location and the damage growth pattern are the two most critical parameters influencing the reliability of the same SHM system applied to identical structural components under the same environmental conditions.

* Corresponding author. Email: fkopsaf@stanford.edu

Structural Health Monitoring, Vol. 15(2), pp. 143-161, 2016.

Introduction

Structural Health Monitoring (SHM) systems utilize distributed, permanently installed sensors at certain structural regions and apply diagnostic algorithms to extract meaningful health information from the sensing data [1-10]. Such sensing data is subjected to various sources of uncertainty associated with all aspects of the inspection environment and operating conditions. In contrast to traditional Non-destructive Evaluation (NDE) procedures, where the factors due to operator pose the dominant uncertainty [11-15], SHM-based technologies are mainly challenged by in-situ effects. These include changing environments (temperature, humidity, and wind), varying operating conditions (ambient loading conditions, operational speed and mass loading, etc.), variation in boundary conditions, sensor and structural aging, and measurement noise amongst others, as well as the sensing network layout itself [16-25]. Usually, the uncertainties due to environmental effects have the largest impact on the system performance. An SHM system needs to be robust to uncertainties, but sensitive enough to detect the required minimum damage even when the sensor data are "corrupted" by these uncertainties. Towards this end, statistical tools and machine learning algorithms are used to effectively tackle the detection and estimation problems [16, 23, 26-32].

SHM technologies, oftentimes in combination with appropriate NDE and/or Health and Usage Monitoring Systems (HUMS), along with sophisticated data management systems and life-prediction models constitute the required steps for the transition to Condition-based Maintenance (CBM). Typically, SHM methods involve the detection, monitoring, evaluation, and assessment of an adverse event that may affect the structural health state. In the current state-of-the-art literature a significant amount of research is targeted to the development of diagnostic approaches based on various sensor technologies [22, 33-35]. These approaches are able to achieve a certain level of capability in terms of detection, evaluation, and assessment of adverse events that can affect the proper structural operation, performance, and safety. However, in order to achieve the verification and validation of the SHM technologies and enable their large-scale applicability, the effectiveness and damage detection sensitivity of any SHM technique must be quantifiable with respect to its ability to accurately determine the actual health condition.

In order to quantify the reliability of an SHM system, it is essential to characterize its sensitivity in terms of the detection capability. In that respect, the first and most critical step is the investigation of the factors and parameters that affect the damage detection sensitivity. Typically, SHM involves four functional levels referred to as Technology Classification Levels (TCL) [36, 37]:

- Level I: Detection of the occurrence of an event
- Level II: Identification of the geometric location of the event
- Level III: Determination of the magnitude or severity of the event
- Level IV: Estimation of the remaining service life/strength (prognosis)

In each level, the technology employed needs to be mature enough in order to effectively accomplish the targeted action. Hence, for any SHM system the targeted TCL has to be defined a-priori with respect to its intended application. A schematic representation of an active sensing SHM system is presented in Figure 1.

The quantification of SHM systems starts from TCL I, as it is of utmost importance to determine whether a system is able to detect an adverse event, such as damage in the form of cracks and delamination, excessive loads, and so on. If an SHM system is not capable of effectively detecting (TCL I) such an adverse event, then higher TCLs would fail to provide reliable results – or in fact achieve any result. Therefore, the TCL I reliability quantification is considered as the most critical task regarding the SHM system quantification. The performance quantification should be always conducted from the lowest to the highest TCL, while the required technology becomes increasingly more complex and challenging for higher TCLs.

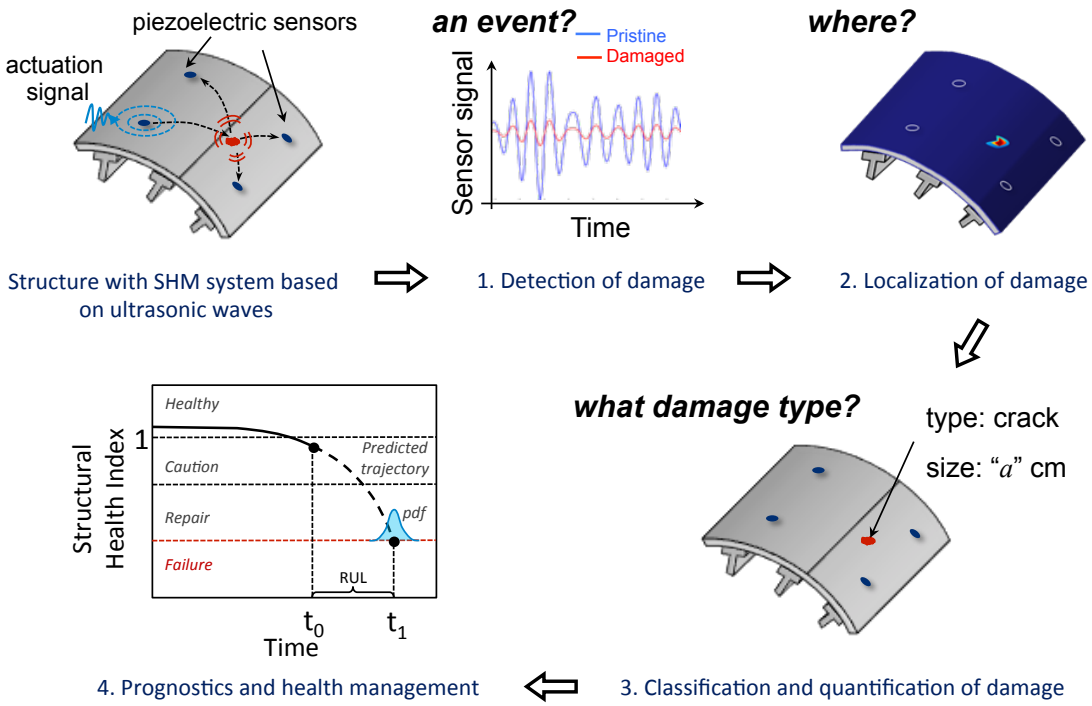

Figure 1: Schematic representation of the generic SHM principles of operation.

Classification of SHM Systems for Reliability Quantification

Typically sensor data may be collected either over predetermined time intervals in a scheduled manner or continuously in an automatic way. Hence, SHM systems are classified with respect to their applicable inspection interval as: (i) Scheduled SHM (S-SHM) systems, in which each inspection is independent of time, and (ii) Automatic SHM (A-SHM), where the monitoring occurs continuously in the time domain [38]. The performance of an SHM system depends upon several key parameters, such as the type, number and location of sensors, the inspection interval,

and the diagnostic algorithms used to process and interpret the sensing data. Apart from the sensor types and diagnostic algorithms, the reliability and accuracy of an SHM system could be significantly influenced by the sensor/actuator network (number and locations of sensors and actuators). However, the sensor network design will depend upon whether the damage location is known (Known Damage Location – KDL) or unknown (Unknown Damage Location – UDL) a priori based on historical data or other preliminary methods of analysis. Hence the sensor network design for KDL (in fact the suspected damage location, also known as "hotspot" monitoring) could be substantially different from those cases where potential damage location is completely unknown, such as the case of random impact damage.

Accordingly, all SHM systems can be classified into four categories as shown in Table 1: (i) KDL S-SHM, (ii) KDL A-SHM, (iii) UDL S-SHM, and (iv) UDL A-SHM. As will be discussed in detail in the following sections, only the case of KDL S-SHM systems may be compared to the reliability quantification of traditional NDE systems as presented in [11-14].

Table 1: Classification of SHM systems based on reliability quantification.

	S-SHM (Scheduled)	**A-SHM (Automatic)**
Known Damage Location (KDL)	The system will only interrogate periodically a known "hotspot" location. *(similar to NDE)*	The system will continuously interrogate a known "hotspot" location.
Unknown Damage Location (UDL)	The system will periodically interrogate the entire structure for damage.	The system will continuously interrogate the entire structure for damage.

Because the working principle in each SHM category is fundamentally different from one to another, it is quite reasonable to assume that a quantification method established for one category may not be applicable directly to the techniques in other categories. For typical NDE techniques, the well-established method of Probability of Detection (POD) has been widely accepted and adopted to quantitatively characterize and evaluate the NDE system's reliability to detect a specified event (damage/flaw) [11-14]. The POD method requires that the location of damage is known (or suspected) and the inspection is performed on a scheduled basis. Therefore, the POD method might be applicable for SHM systems falling into the top-left quadrant of Table 1 corresponding to KDL S-SHM systems.

Accordingly, in this study, the case of SHM systems falling in the KDL S-SHM category will be considered. Continuous monitoring and unknown damage location situations will not be considered and evaluated. In the current literature, there are a very limited number of studies addressing the SHM reliability quantification [37-45].

Comparison of NDE and SHM Systems

For the reliability quantification of traditional NDE techniques the POD method is an established and widely applied approach [13]. POD is defined as the probability of detecting an event or flaw (crack, delamination, etc.) of a specific target size *a* (damage or any other meaningful feature that should be explicitly defined and be unambiguously measurable) under specified inspection procedures and environmental conditions [11-14]. Practically, the NDE POD is presented as the curve generated by POD values as a function of the flaw size *a.* It represents the probability of detecting a specific flaw type with a representative flaw size *a.* As the POD is a statistical quantity, it is also associated with a certain confidence level (CL). Therefore, depending on the requirements of the specific application, the desired POD/CL values define the targeted quantification goal. In general, the values 90/95, representing a POD=0.9 (90%) with a CL=0.95 (95%), are most commonly employed in practice.

Although there are many similar physical working principles between NDE and S-SHM systems, the key difference [37-40] is that NDE techniques use a probe(s) or transducers that is (are) movable, but typical SHM techniques do require the sensors and actuators to be fixed and permanently installed onto the structure. In that respect, methods on the diagnosis [46] and compensation of sensor degradation [47] have been proposed.

POD Estimation for NDE Systems

For an NDE system, the POD is defined as the proportion of all flaws of a representative size *a* (POD*(a)*) that will be detected by the NDE technique when applied by trained inspectors to the population of structural elements in a well-defined environment. Demonstrating the capability of the NDE system for a specific application requires a number (several trials, several operators) of carefully controlled experiments followed by a valid statistical analysis of the resulting data. To reflect the statistical uncertainty within the obtained POD values from different trials, a CL can be calculated yielding the POD/CL characterization of capability. POD calculation procedures are generally applied to estimate the minimum size of flaws that can be detected at a certain POD/CL value.

Depending on the criticality of the application, the POD of a flaw of size *a* can be estimated at different confidence levels. Typically, the value $a_{90/95}$ is chosen as the standard for system design and implementation. Thus, an $a_{90/95}$ crack size characterization means that there is 95 percent confidence that at least 90 percent of all cracks of size $a_{90/95}$ will be detected. The importance of this POD procedure is that it can quantify the largest flaw that could be missed in the inspection and the minimum flaw size that could be detected with a 90/95 POD/CL. The general procedure to determine the POD(*a*) for a specific NDE technique starts with creating a list of variables that influence the system's performance. Variation in NDE system response (and, hence, uncertainty in flaw detection) is caused by the physical attributes of the flaws under test, the NDE process variables, system settings, and test protocol.

The uncertainty caused by differences between flaws is accounted for via the use of representative specimens with flaws of known size in the demonstration inspections. The uncertainty caused by the NDE process is accounted for by a test matrix of different inspections to be performed on the complete set of specimens. The test matrix is a list of planned process test conditions which collectively define one or more experiments for assessing the NDE system capability. Thus, the test matrix is created using as many combinations of these variables as feasible [13]. In general, the actual number depends on the number of parameters needed to obtain a representative specimen. If a smaller number of variables is considered, this will be reflected as a considerable uncertainty in the parameter estimates, which will cause wider confidence bounds on the POD(a) curve and a larger value for the $a_{90/95}$.

The precision of the POD(a) function depends on the number of inspection specimens with flaws, the size of the flaws, and the type of inspection results (*hit/miss* or *â-vs-a*). Larger sample sizes will, in general, provide greater precision in the estimate of the POD(a) function, and thus provide a more accurate value for $a_{90/95}$. The sample size is determined from the number of flaws in the experiment. In addition, unflawed inspection sites are necessary in the specimen set to preclude guessing and to estimate the rate of false indications. For hit/miss analysis, studies suggest a minimum of 60 flaws to be used to estimate the POD(a) function. When the NDE system outputs a quantitative response, $\hat{a}$, that can be correlated to the flaw size, the data are known as *â-vs-a* inspection results and an advanced POD(a) analysis is available. For *â-vs-a* analysis a minimum of 40 flaws should be used to estimate the POD(a) function. The recorded signal response, $\hat{a}$, provides significantly more information for analysis than a simple hit/miss inspection response. The POD(a) function is derived from the correlation of the *â-vs-a* data, and the pattern of $\hat{a}$ responses can be used for extrapolation. More precise estimates of a_{90} and narrower confidence bounds on the POD(a) curve result from target sizes that are uniformly spaced on a Cartesian scale and therefore this is the recommended practice. In addition, flaws which are so large that they are always found or so small that they are always missed (or produce a signal which is dominated by the system noise) provide only limited information about the POD(a) function [13].

POD curves are routinely generated for NDE methods and typically involve a large numbers of measurements to capture uncertainties arising from variations in operators, probes, data acquisition hardware and software, structural properties (geometry, material, surface finish), and flaw morphology and propagation (flaw type, shape, orientation, depth, location, etc.). Due to those uncertainties in the NDE inspection process, POD analysis evaluated at different instances may result in different values and therefore need to be considered within a statistical framework.

The NDE POD approach for SHM quantification

Historically, the POD determination begins with crude binary methods, while contemporary analysis relies on Linear Models (LM) that constitute the theoretical basis for the *â vs a* analysis [13]. For *â vs a* linear model of the form $y = \beta_0 + \beta_1 x + \varepsilon \implies \boldsymbol{y} = \mathbf{X} \cdot \boldsymbol{\beta} + \boldsymbol{\varepsilon}$ (in vector/matrix

notation), with $y = \hat{a}$ (or *log(â)*), $x = a$ (or *log(a)*), β_0, β_1 designating the model parameters, and ε a random error (Gaussian, zero mean with variance σ^2 sequence), there are four main assumptions, aligned with linear regression analysis, that need to be satisfied [13]:

1. Linearity of the model parameters: $E(y_i|\mathbf{X}) = \boldsymbol{x}_i \cdot \boldsymbol{\beta}$, where $\boldsymbol{x}_i$ is the i-th row of $\mathbf{X}$
2. Uniform variance (homoscedasticity): $\text{var}(y_i|\mathbf{X}) = \sigma^2, \quad i = 1, \dots, n$
3. Uncorrelated observations: $\text{cov}(y_i, y_j|\mathbf{X}) = 0, \quad i \neq j$
4. Normal errors: $(y_1, y_2, \dots, y_n)|\mathbf{X}$ have a multivariate normal distribution

If *any* of these assumptions is violated the subsequent analysis will be invalid and will result in erroneous results. Figure 2 presents indicative *â vs a* data, with respect to the measured crack length (*a*) and the corresponding damage index (DI, also referred to as *â*). More specifically, Figure 2 shows the crack length vs DI plot of a system that satisfies the linear model assumptions 1-4. In this case, the underlying POD analysis is valid and will yield correct results. If the POD procedure is properly designed and implemented, as described in [13], its outcome should resemble the graph of Figure 2. On the other hand, if some of the linear regression assumptions are not satisfied then the underlying POD analysis would not be valid. In this case, appropriate and oftentimes more sophisticated statistical methods and corresponding models may be employed [48, 49].

In SHM systems, data are usually collected from the same component and compared with the previously recorded data [37, 49]. In addition, the obtained data are potentially affected by varying enviromental and/or operating conditions. The NDE guidelines for POD estimation approach as described in MIL-HDBK-1823A are valid only in the case of independent data [13]. The distinction between dependent and independent data is very important considering current NDE standards for validation. Ignoring the data dependency assumption may lead to erroneous POD estimation due to biased standard error and confidence intervals estimates.

Figure 3 presents indicative damage index versus the crack length results as obtained from an SHM system in a recent study [49]. The results correspond to experiments on three samples of a wing attachment lug. Fatigue cracks were initiated and grown in the lug by loads applied through the hydraulic actuator attached to the end of the wing spar. In this case a single pair of sensor-actuator was employed. Unlike the data of Figure 2, in this case a substantial variability both across and within specimens is evident. In this case, the SHM results, as reflected on the damage index versus crack length plots, indicate data dependency on each individual specimen. Such differences could be attributed to differences in material, or other properties related to those particular specimens, the experimental setup, or the specific computations used to define the response signal [49].

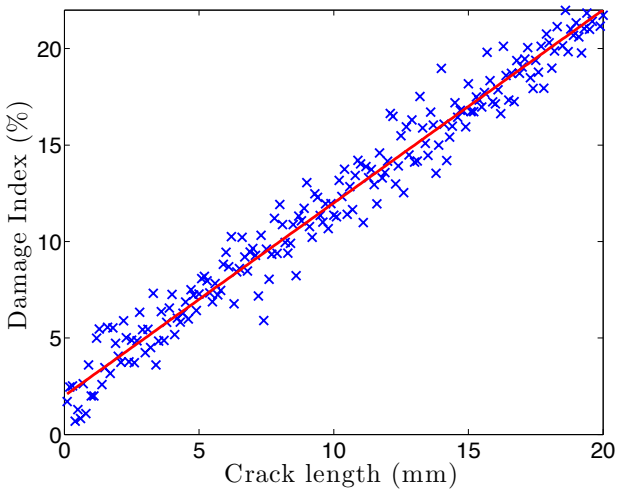

Figure 2: Indicative damage index versus crack length for NDE *â-vs-a* POD analysis. The red line corresponds to the estimated linear regression model fitted to the obtained data. The more the damage index values that correspond to measured crack lengths the higher the accuracy of the POD estimation.

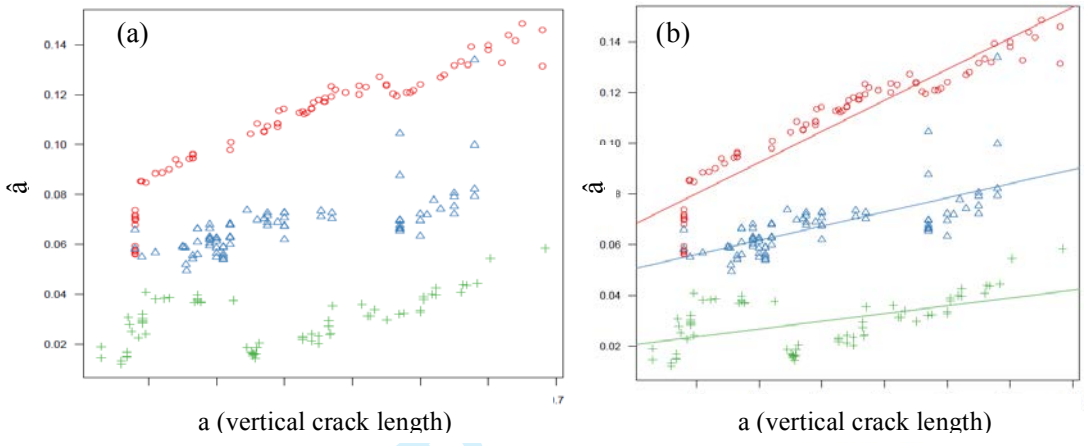

Figure 3: Scatterplot of the vertical crack length vs. damage index for each of three wing attachment lug specimens (each color corresponds to a different wing lug specimen): (a) without and (b) with fitted linear regression lines. For the detailed description of the experimental process see [49].

Therefore, before quantifying a KDL S-SHM system, it is necessary to study and characterize all these factors affecting the damage detection sensitivity. The interest is to identify the critical parameters that affect such an SHM system and study the damage detection results as reflected in the sensing signals and the obtained damage indices.

In order to generate typical DI vs damage size (notch length) curves, thirty "identical" test structures, each outfitted with the exactly same SHM system (sensors, hardware, and diagnostic algorithm), were used in the test study. The objective is to determine whether the DI data generated from these coupons meet the requirements and assumptions of the traditional NDE approach for POD estimation. In addition, both numerical simulations and analytical methods

were performed to explore and determine the parameters that may affect the DI values and the corresponding detection sensitivity of the SHM system.

The Coupons and the Experimental Setup

A number of experiments were conducted on thirty identical Aluminum coupons of dimensions 12" (300 mm) × 6" (200 mm) Al 2024-T3 with a hole in the center. The experimental geometric configuration is shown in Figure 4. Two single-PZT SMART Layers® (type PZT-5A) designed and fabricated by Acellent Technologies were attached on the stiffener plate, as shown in Figure 4, using Hysol® EA 9394 adhesive. The employed PZT actuator/sensors are ¼" in diameter and 10 mm in thickness. The ScanGenie® data acquisition hardware and SmartComposite™ software were used to carry out the experiments using a pitch-catch setup. A five-peak tone burst actuation voltage signal with a center frequency of 250 kHz was driven to PZT #1. The response was recorded at PZT #2.

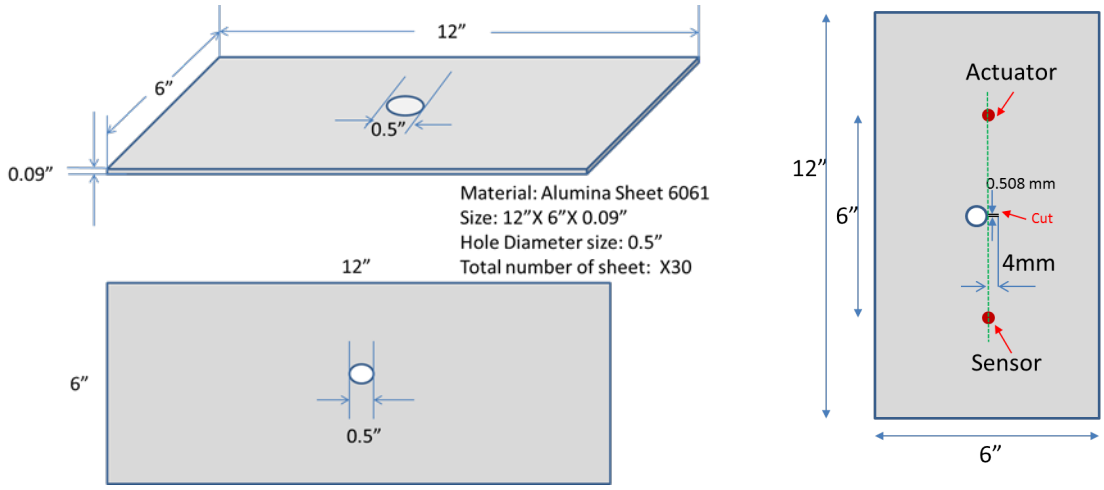

Figure 4: Dimensions of the Aluminum coupon equipped with PZT-5A type piezoelectric sensors on the surface using Hysol® EA 9394 adhesive.

The Aluminum coupon dimensions are shown in Table 2 and are the same for both the numerical simulations and experimental tests. Figure 5 presents the thirty identical coupons that were prepared to investigate the effects of different system parameters on the sensor signals. To simulate the practical installation and mounting procedure and estimate the induced uncertainty in the different system parameters, six technicians attached one actuator-sensor pair on each of five coupons that they were assigned. The thirty identical coupons were used to measure the variation in the system parameters, including the percentage variation on the PZT properties, thickness of adhesive, and actuator-sensor locations. After estimating the variation resulted from the actual experimental testing, additional numerical wave propagation studies were carried out.

Each of these system parameters was assessed both individually and collectively in order to study the effect of each individual system parameter on the sensor signal and damage index.

Table 2: Dimensions of coupons, PZT sensors, and adhesive.

Thickness of Aluminum	2.286 mm
Thickness of PZT sensor	0.25 mm
Diameter of PZT sensor	6.35 mm
Thickness of adhesive	0.05 mm
Diameter of hole	12.7 mm
Length & width of plate	304.80 mm x 152.40 mm

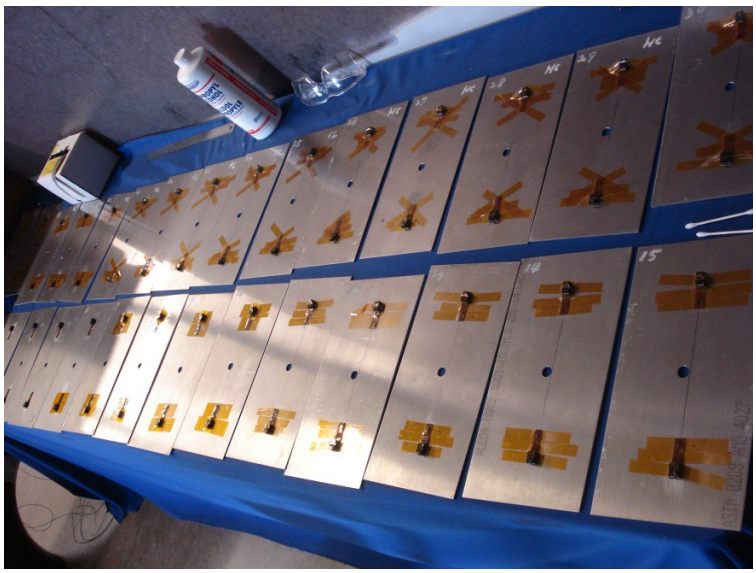

Figure 5: Thirty coupons outfitted with identical pairs of piezoelectric actuators-sensors.

Analytical Investigation: Effect of Sensor Properties on the Damage Index

In this section, the effect of the variation of the sensor properties on the damage index is analytically investigated. Note that a two-dimensional structure is considered to simplify the theoretical analysis. Variations in the environmental and operating conditions between the baseline and inspection data records have not been taken into account in the following analysis. Moreover, a single guided wave mode generation is assumed. Figure 6 shows the schematic of the incident, reflected and transmitted waves between the actuator and the sensor along a plate with a notch.

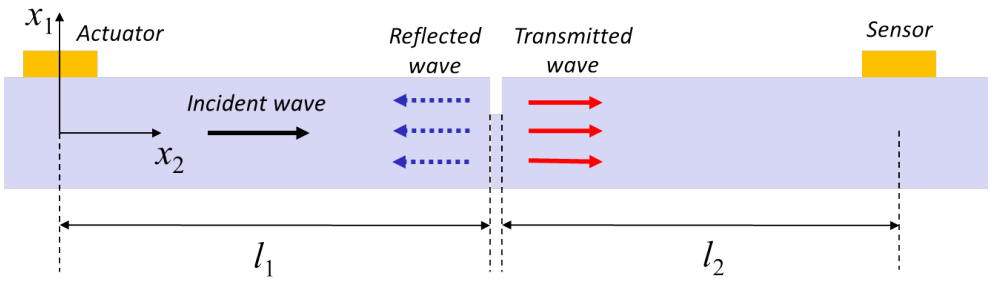

Figure 6: Schematic of the incident transmitted and reflected waves along a plate with a notch.

Based on [50] the amplitude of the incident mode *i* at the sensor location (A_{it}) and amplitude of the transmitted converted mode *m* at the sensor location (A_{mt}) are defined as follows:

$$A_{it} = T_i A_i e^{-k_i(l_1+l_2)}, \;\; A_{mt} = T_m A_i e^{-(k_i l_1 + k_m l_2)}. \tag{1}$$

T_i and T_m correspond to the transmission coefficients of the i^{th} mode and the transmission coefficient of the i^{th} mode to the m^{th} mode, respectively. T_i and T_m are dependent on the depth of the notch. A_i is the amplitude of the incident mode i at the sensor location. l_1 and l_2 are the distance between the actuator and the notch, and the distance between the notch and the sensor, respectively. The width of the notch is assumed to be negligible. k_i and k_m correspond to the wave attenuation of the i^{th} mode, and the wave attenuation of the m^{th} mode converted from the i^{th} mode, respectively.

By modeling the piezoelectric sensor as a capacitor, the output voltage of the piezoelectric sensor is defined as the ratio of the accumulated charge (Q_p) to the capacitance value (C_p) of the piezoelectric sensor [8]:

$$V_{out}(n) = \frac{Q_p}{C_p} = \frac{Y_s h_s g_{31}}{2c} \int \varepsilon_{ii} \, dl \tag{2}$$

where Y_s is Young's modulus of the sensor, and h_s and $2c$ are the thickness and length of the sensor, respectively. g_{31} is the *xz*-directional piezoelectric voltage constant and ε_{ii} is the sum of the strains at the sensor location.

Once Eq. (1) is plugged into Eq. (2), the output voltage of the baseline data (no notch) and that of the inspection data (with notch) are derived as follows:

$$V_{Baseline}(n) = \left(\frac{Y_s h_s g_{31}}{2c} \int_{l_1+l_2-c}^{l_1+l_2+c} A_i e_i^{-i2\pi\mu_i x_2} dx_2 \right) \cdot V_{in}(n)$$

$$V_{Inspection}(n) = \left(\frac{Y_s h_s g_{31}}{2c} \int_{l_1+l_2-c}^{l_1+l_2+c} (A_{it} e^{-i2\pi\mu_i x_2} + A_{mt} e^{-i2\pi\mu_m x_2}) dx_2 \right) \cdot V_{in}(n) \tag{3}$$

From Eq. (3), the normalized mean squared error based damage index, which is generally used to compare two signals, can be derived as follows:

$$DI = \frac{\sum_{n=1}^{N}\left(V_{Inspection}(n) - V_{Baseline}(n)\right)^2}{\sum_{n=1}^{N} V_{Baseline}(n)^2} = \frac{\left[\int_{l_1+l_2-c}^{l_1+l_2+c}\left\{\left(\frac{A_{it}}{A_i}-1\right)e^{-i2\pi\mu_i x_2} + \frac{A_{mt}}{A_i}e^{-i2\pi\mu_m x_2}\right\}dx_2\right]^2}{\left(\int_{l_1+l_2-c}^{l_1+l_2+c} e^{-i2\pi\mu_i x_2}dx_2\right)^2} \quad (4)$$

Equation (4) clearly shows that the sensor properties are cancelled out during the damage index calculation. Furthermore, it proves that the DI solely depends on the coefficients related to the guided wave propagation. This is a very significant result in agreement with the numerical simulations of the next section.

The damage detection sensitivity characterization of any SHM system requires understanding of the way the various system parameters affect the sensor signals. Once the effects are understood and properly quantified, it is crucial to select a damage index that is insensitive to all other environmental and external factors other than damage. The damage index that is highly sensitive to damage and much less sensitive to other external factors will be selected for detecting, localizing, and characterizing the damage presence on the structure. Therefore, the damage detection sensitivity of the SHM system depends highly on the appropriate selection of the damage index.

The Damage Index (DI)

Various system parameters that could affect the signals are identified through experimental and numerical simulation results. Both simulations and experiments were carried out for thirty isotropic Aluminum coupons. Metallic homogeneous coupons were selected for this preliminary testing since the focus of this study is the investigation of the effect of uncertainties of the sensor/actuator installation, and the material properties of sensor, adhesive, and structure the on sensor signals.

The damage index used in this work is defined as:

$$N_{dmg} = \frac{C_{sig}}{\sqrt{\sum C_{sig}^2}}$$

$$N_{ref} = \frac{\sum(B_{sig}\cdot N_{dmg})}{B_{sig}\cdot \sum B_{sig}^2}$$

$$DI = \sum\left(N_{dam} - N_{ref}\right)^2 \quad (5)$$

with B_{sig} designating the pristine signal, C_{sig} the damage signal, N_{ref} the normalized pristine signal, and N_{dam} the normalized damage signal.

After careful consideration, the damage index was selected in such a way that it has high sensitivity to damage growth (damage size and orientation) and less sensitivity to other factors (such as material properties of adhesive, PZT and structure, variation on adhesive thickness, etc.).

Numerical Simulations

SHM and damage diagnosis often require multi-scale electro-mechanical simulations to analyze the signal (often ultrasonic waves) propagation on the structural substrate. The wave propagation simulations used to be performed almost exclusively using the Finite Element Method (FEM), which requires a very fine spatial discretization to simulate the high-frequency nature of waves from the piezoelectric sensors, which results in high computational cost [51, 52]. On the other hand, the Spectral Element Method (SEM), originally developed by Patera [53] in the mid-1980s, is a similar numerical method to find approximate solutions of partial differential equations, but does not require as a fine mesh to get results of desired accuracy, and is computationally less expensive than FEM.

A multi-physics SEM-based simulation tool, the Piezo Enabled Spectral Element Analysis (PESEA) code, was developed in the Structures and Composites Laboratory (SACL) at Stanford University to solve the governing partial differential equations in ultrasonic wave propagation problems [3, 54, 55]. PESEA is capable of efficiently solving the coupled electromechanical problems that occur in smart structures with embedded or attached piezoelectric sensors and actuators. Varying environmental and operating conditions, such as temperature variation [4, 16, 25, 56] and applied loads [25, 55], which otherwise influence the signal propagation, can also be effectively modeled by taking into account the non-linearity in the stress-strain relationship.

Though formulation of SEM is very similar to that of FEM, it uses high-order elements with nodes defined at Gauss-Lobatto-Legendre (GLL) points. As an example, a solid spectral element of order 4×4×4 is shown in Figure 7. High-order shape functions and nodal quadrature make the simulation more accurate and faster than linear FEMs. Hence, PESEA is used to model piezo-induced acousto-ultrasonic wave propagation in structures with complex geometries. The attenuation in the viscoelastic material is implemented by introducing Rayleigh damping. PESEA was also extended to include the capability of simulating Lamb waves in solid media with dispersion, attenuation and anisotropy, which is a problem prominent in composite materials. The formulation of the Layered Solid Spectral Element (LSSE), with the included Rayleigh viscous damping model, was developed [3, 54] to accurately and efficiently simulate ultrasonic wave propagation and sensor response in laminated composites. PESEA can also be used to model ultrasonic wave propagation in complex structures with damage, such as cracks in metallic structures and debonds/delaminations in composite structures. The effectiveness of PESEA in simulating Lamb wave-based detection of composite delamination was validated using structures

of complexity varying from a model of a simple flat composite plate with a delamination, to composite structures with complex geometries like a stiffened panel [3, 54].

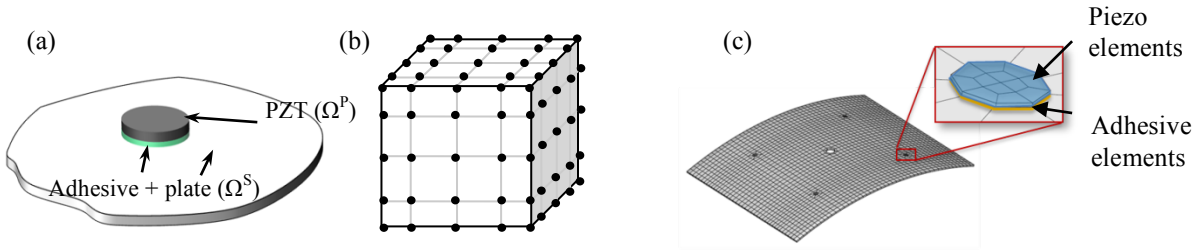

Figure 7: (a) Plate with piezoelectric sensor mounted on the surface using adhesive; (b) solid spectral element of order 4×4×4, and (c) modeling of piezoelectric transducers and adhesive layers.

In this work, PESEA will be the computational tool based on which the numerical simulation of ultrasonic wave propagation and the piezoelectric sensor response will be obtained. Extensive PESEA simulations have been performed for the investigation of the effect of various SHM system parameters on the response signals and the damage index, as well as the way system uncertainties propagate and affect the reliability analysis. More specifically, in this study we address the effects of: (i) sensor, structural, and adhesive material property variations on the damage index, (ii) uncertainty in the sensor installation on the DI including both the variation on the adhesive thickness and the location of the sensors, and (iii) damage propagation and morphology on the DI including the effects of the damage size growth and damage orientation.

The experimentally obtained response signals were compared with the corresponding obtained via the PESEA tool, in which solid spectral elements of order 5×5×3 were used. The adhesive thickness was assumed to be 50 μm. Traction free boundary conditions were assumed and the excitation was applied to the top surface nodes of PZT #1 (actuator). Indicative simulated response signals for PZT #2 (sensor) are compared with experimental signals in Figure 8. The PESEA-based simulated signals match very well with the corresponding experimental signals. In the past, PESEA was validated on isotropic and anisotropic plates attached with stiffeners [54].

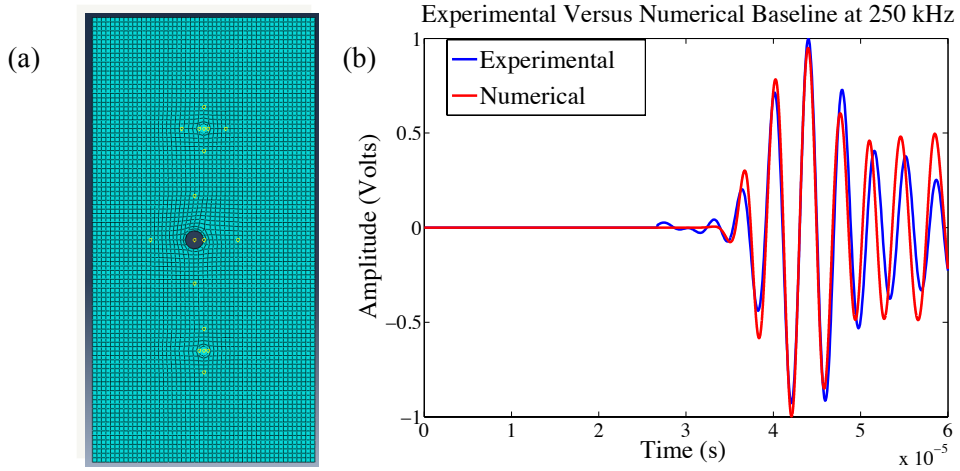

Figure 8: (a) Mesh for the geometry created in Abaqus CAE; (b) Comparison between indicative experimental and simulated signals.

A few snapshots of the FEM models corresponding to the pristine and damaged coupons are presented in Figure 9.

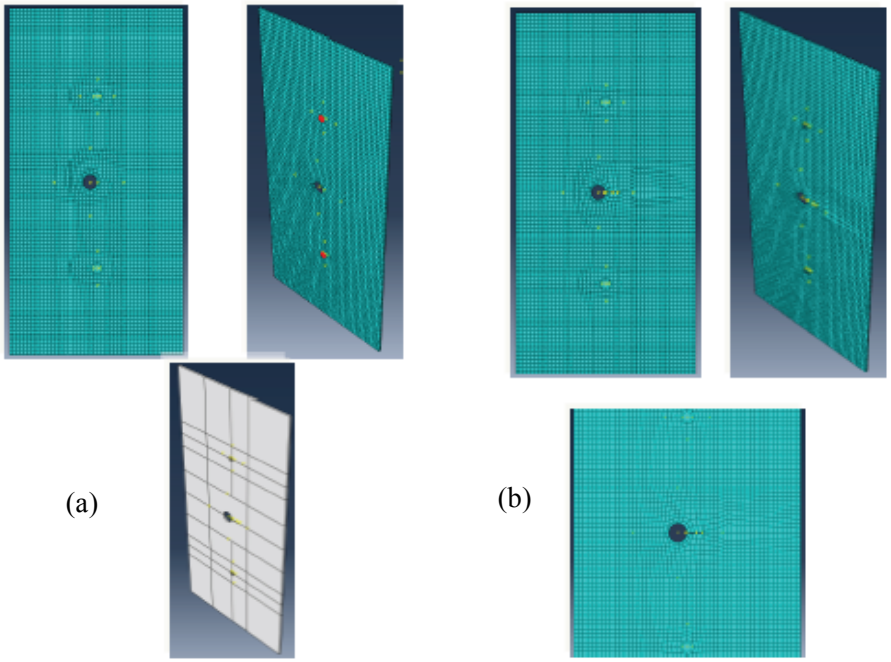

Figure 9: Schematic of the SEM mesh of simulated (a) pristine coupons, and (b) damaged coupons.

Damage Detection Sensitivity Characterization Results

For the characterization of the damage detection sensitivity, the following parameters are considered, while their effect on the sensing signals and the damage index is investigated. The seven parameters considered in this work are grouped into three categories:

- *Effect of variation in material properties on damage index*
    1) Variation in PZT properties

2) Variation in properties of the structural material
3) Variation in properties of the adhesive

- *Effect of uncertainties in sensor (SMART Layer) installation on damage index*
  4) Variation in adhesive thickness
  5) Variation in sensor location
- *Effect of damage propagation on damage index*
  6) Damage size
  7) Orientation of damage

The objective of this section is to collect information and investigate the way the variations of the above parameters affects the damage index. The percentage variation (in PZT properties, adhesive properties, structural properties etc.) is calculated with respect to the mean value of their properties. The general properties of the materials used in the wave propagation simulations are presented in Table 3. Table 4 enlists the mean properties of aluminum, adhesive, and PZT, whereas Table 5 summarizes the factors and the corresponding variations considered to affect the damage index in the numerical simulations.

Table 3: General properties of the materials used in the simulations.

Adhesive	Hysol EA-9696; Thickness: 0.05 mm; Density: 1100 kg/m^3
Aluminum 6061	Thickness: 2.286 mm; Density: 2700 kg/m^3
PZT	Thickness: 0.25 mm. diameter 6.35mm; Density: 7750 kg/m^3

Table 4: Material properties of aluminum, PZT, and adhesive.

Material	**1: Aluminum 6061**			**2: PZT**			**3: Adhesive**		
Density	2700			7750			1100		
Young's Moduli E11, E22, E33 [GPa]	68.9	68.9	68.9	60.97	60.97	53.19	2.6	2.6	2.6
Shear Moduli G23, G31, G12 [GPa]	26	26	26	21.05	21.05	22.57	1	1	1
Poisson's Ratios v23, v13, v12	0.33	0.33	0.33	0.4402	0.4402	0.35	0.3	0.3	0.3
Electromechanical coupling coeff [D11,D12,D13,D14,D15,D16] [D21,D22,D23,D24,D25,D26] [D31,D32,D33,D34,D35,D36]				[0.0,0.0,0.0,0.0,558.0e-12,0.0] [0.0,0.0,0.0,558.0e-12,0.0,0.0] [-171.0e-12,-171.0e-12,374.0e-12,0.0,0.0,0.0]					
Dielectric constant: EPS11,EPS22,EPS33 (related to capacitance)				1730	1730	1700			

Table 5: Factors considered in the numerical simulations for the characterization of the damage detection sensitivity.

#	Parameter	How many variations are to be considered during simulation	How to vary properties/damage size etc.,	Number of simulations	Outcome
1	Damage size	0, 2, 4, 6, 10, 14, 20 mm		210	Effect of damage size on DI
2	Orientation of damage	(6 mm damage case) 0°/15°/30°/45°		4	Effect of damage orientation on DI
3	Percentage variation on PZT properties	±5% from mean for mechanical properties ±20% for electrical (capacitance) and electro-mechanical (D11,D12,D13,…,D33) coupling coefficients	Random selection of each property within this variation	30	Effect of PZT property variation on DI
4	Percentage variation on properties of structural material	±3% from mean	Random selection of each property within this variation	30	Effect of structural property variation on DI
5	Percentage variation on thickness of adhesive	±50% from mean	Random variation	10	Effect of adhesive thickness
6	Percentage variation on properties of adhesive	±2% from mean	Random selection of each property within this variation	30	Effect of adhesive property variation on DI
7	Percentage variation on location of sensor (during installation)	±2 mm from mean	Random variation	10	Effect of variation on sensor location on DI
Total				324	

Effect of variation in material properties

Variation in sensor properties. Based on the PZT manufacturer's recommendation, ±20% random variation in dielectric constants and ±20% random variation in electromechanical coupling coefficients along with ±5% random variation in PZT's mechanical properties were implemented in the numerical wave propagation simulations. Figure 10 shows the variation in sensor signals collected (experiment) and numerically generated (simulation) along with the measured capacitance variation (experimental), and the range of dielectric constants estimated using a ±20% random variation in the mean properties. A significant variation in the baseline signals was observed from both the measured and simulated sensor signals. Even with this

variation in the baseline sensor signals, the calculated damage index for the thirty coupons showed a negligible variation, which is due to its insensitivity to the variation in the sensor properties. In addition, the variation of these sensor signals is cancelled out by subtracting the baseline (pristine coupon) sensor signal from the current (damaged coupon) sensor signals.

Figure 12(a) shows the damage index variation for 30 coupons (used in the simulations). The DI variation is negligible, and thus we can conclude that the variations in the sensor properties will not affect the selected damage index.

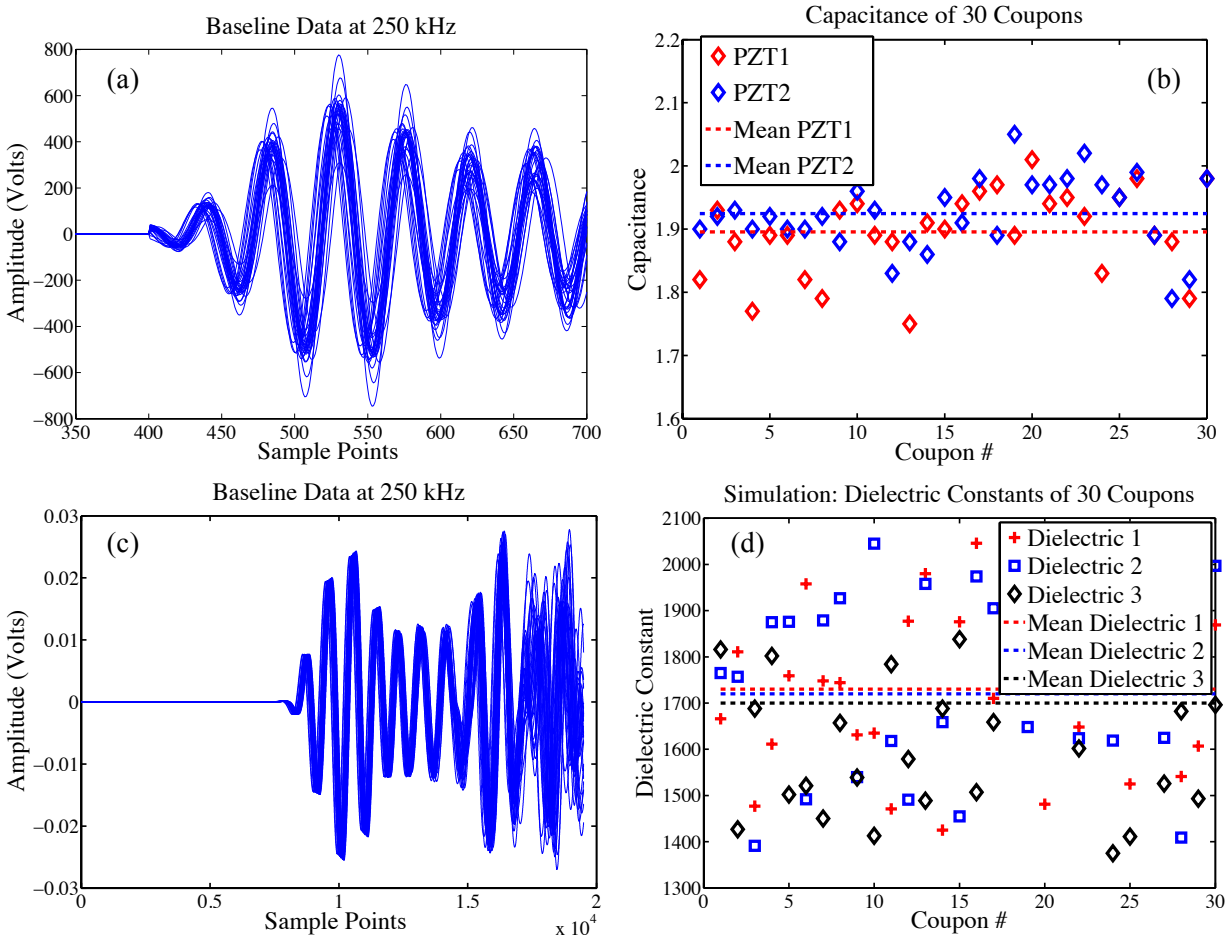

Figure 10: Variation in baseline sensor signal for thirty pristine coupons: (a) variation in experimental signals, (b) measured capacitance (experiments), (c) variation in numerical signals, and (d) dielectric constants (simulations).

Variation in structural properties. In this case, a ±2% random variation in structural properties was implemented in the wave propagation numerical simulations. Figure 11(a) presents the variation of the simulated baseline sensor signals. A significant variation in the baseline signal amplitude and phase was observed. However, the damage index estimated from the thirty coupons yields a negligible variation, as it is insensitive to variations in structural properties.

Similarly, the variation in these sensor signals is cancelled out by subtracting the baseline (pristine coupon) sensor signal from the current (damaged coupon) sensor signal

Figure 12(b) shows the variations in the DI for the thirty coupons (from simulations). The variation is negligible and as a result we may infer that variation in the structural property will not affect the damage index.

Variation in adhesive properties. In this case, a ±2% random variation in the adhesive properties was implemented in the numerical wave propagation simulations. Figure 11(b) presents a negligible variation in the baseline sensor signals that were numerically estimated. Hence, the estimated damage indices exhibit a negligible variation; again the selected damage index is insensitive to the variation on adhesive properties.

Figure 12(c) shows the negligible variation in the damage indices obtained from thirty coupons via simulations due to the variation in adhesive properties. Hence, it is concluded that variations in the adhesive properties does not affect the damage index calculation.

In summary, the effect of variations in the material properties has a minimum or even negligible effect on the selected damage index.

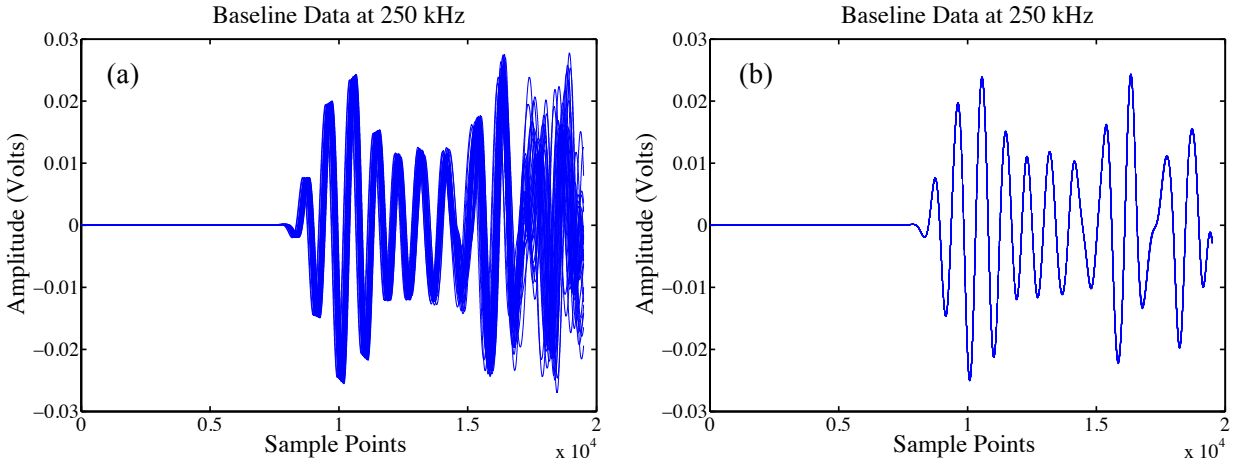

Figure 11: Numerical simulation results (thirty pristine coupons): (a) Variation in sensor baseline signal due to variation in the structural properties; (b) Variation in sensor baseline signal due to variation on the adhesive properties.

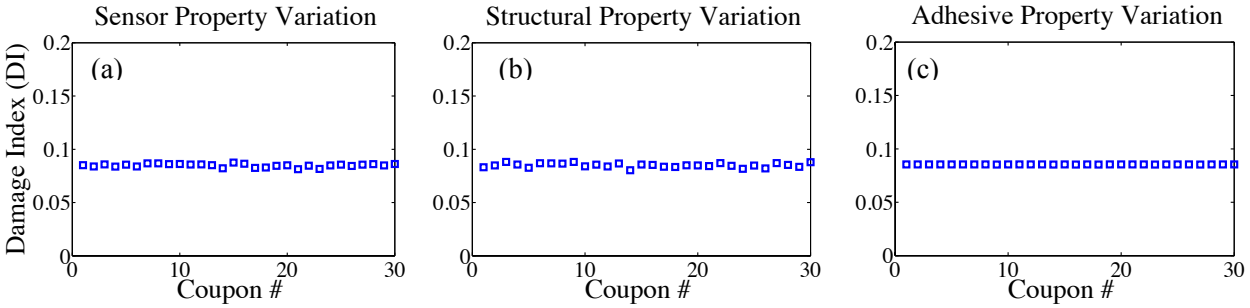

Figure 12: Numerical simulation results on the effect of variation in the material properties on the DI: (a) effect of variation in sensor properties, (b) effect of variation in structural properties, and (c) effect of variation in adhesive properties.

Effect of sensor installation variation

Variation in adhesive thickness. Based on the measured adhesive thickness of thirty identical experimental coupons, variations in adhesive thicknesses are estimated approximately ±50% from the mean adhesive thickness. Therefore, a ±50% random variation in the adhesive thickness was implemented in the numerical simulations. Table 6 shows the randomly selected adhesive thicknesses that were used in the numerical simulations. In order to minimize the computational time required by the modeling and computational efforts, ten different coupons were simulated in this case. Figure 13(a) presents the variation in the baseline sensor signals that were numerically estimated. Figure 13(b) shows the numerically estimated damage indices. A small variation (1.18%) in the damage index is observed that is due to the ±50% variation in adhesive thickness. Hence, the conclusion is that variations in the adhesive thickness might not severely affect the damage index.

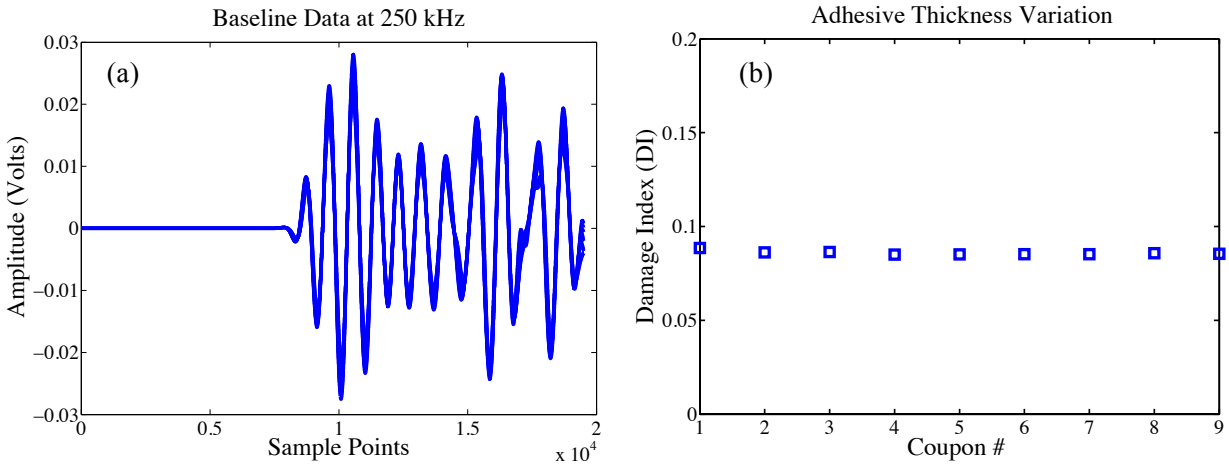

Figure 13: Numerical simulation results (10 pristine coupons): (a) Variation in baseline sensor signals due to variation in the adhesive thickness; (b) Effect of variation in adhesive thickness on the DI.

Table 6: Variation in the adhesive thickness.

#Set	Thickness (mm)
1	0.0357
2	0.0706
3	0.0739
4	0.0322
5	0.0378
6	0.0451
7	0.0463
8	0.0523
9	0.0602
10	0.0522

Variation in sensor location. Based on the measured center of the PZT locations on the thirty identical experimental coupons, the variation in the sensor location is estimated to be approximately ±5 mm from the mean PZT location. Table 7 shows the measured variation of the actuator and sensor locations on the actual test coupons. Figure 14 schematically presents the variation in the actuator-sensor locations of the thirty test coupons. In this case, a ±5 mm random variation in the PZT sensor locations was implemented in the numerical simulations. Similarly, in order to minimize the required computational burden and time, ten coupons were simulated. Figure 15(a) presents the variation of the simulated baseline sensor signals. Figure 15(b) shows the estimated DI that exhibits a maximum 10.84% variation in its value resulting from the ±5 mm variation of the actuator-sensor locations. In this case, the analysis demonstrates that variations in the sensor-actuator location have a significant impact on the damage index.

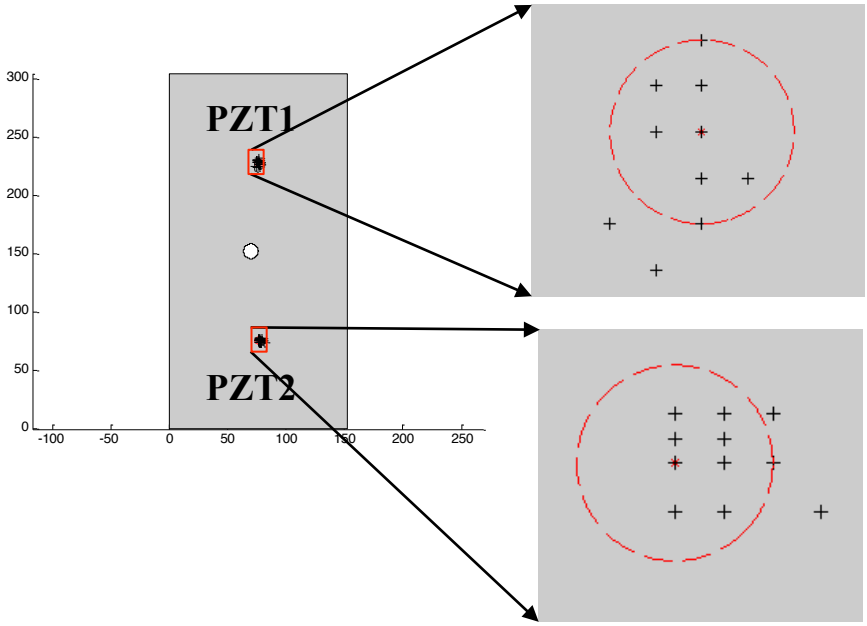

Figure 14: Variation on actuator-sensor locations in 30 test coupons.

Table 7: Variation in sensor location.

Max & Min error in the sensor location (in mm)			
Max error in X-Y directions (PZT1)		Max error in X-Y directions (PZT2)	
3.175 (X)	4.76 (Y)	4.76 (X)	1.58 (Y)

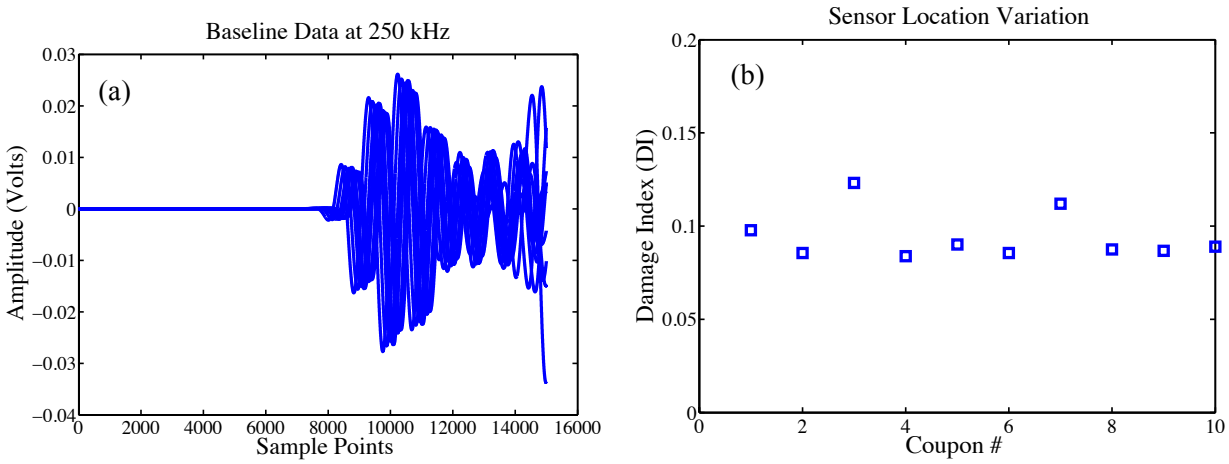

Figure 15: Numerical simulation results (10 pristine coupons): (a) Variation in baseline sensor signal due to variation in sensor locations and (b) effect of variation in sensor location on DI.

Effect of damage propagation

Variation in damage size. In this study, six different damage sizes (notch lengths of 2mm, 4mm, 6mm, 10mm, 14mm, and 20mm) were selected for the numerical simulations and four different damage sizes (notch lengths of 2mm, 4mm, 6mm, and 10mm) were selected for the experimental destructive tests. Table 8 presents the variation in the damage index with respect to the six simulated damage sizes. The damage index variation for the thirty simulated and experimental cases is shown in Figure 16. It is evident that the values for increasing damage size are, as expected, also increasing for both the numerical and experimental data. However, the standard deviation of the DI for experimental data is much higher than that for simulation data. The main reason for this is that the damage orientation for the simulations is horizontal, whereas for the real experiments the orientation (shown in Figure 18) was varied significantly which resulted in higher deviation in the DI. Figure 17 presents the variation of the damage index that is due to the damage size variation for both the simulated and real experimental damage cases. In this case the larger damage index variation due to the real damage is evident.

Table 8: Effect of damage size on the DI.

	Damage index variation due to damage size					
	2 mm	**4 mm**	**6 mm**	**10 mm**	**14 mm**	**20 mm**
Mean	0.0238	0.0577	0.0849	0.2628	0.481	0.7566
Std. deviation	0.0006	0.0014	0.0019	0.0066	0.0081	0.0094
Maximum	0.0251	0.0606	0.0885	0.2789	0.5007	0.7745
Minimum	0.0221	0.0543	0.0802	0.2449	0.4631	0.7298

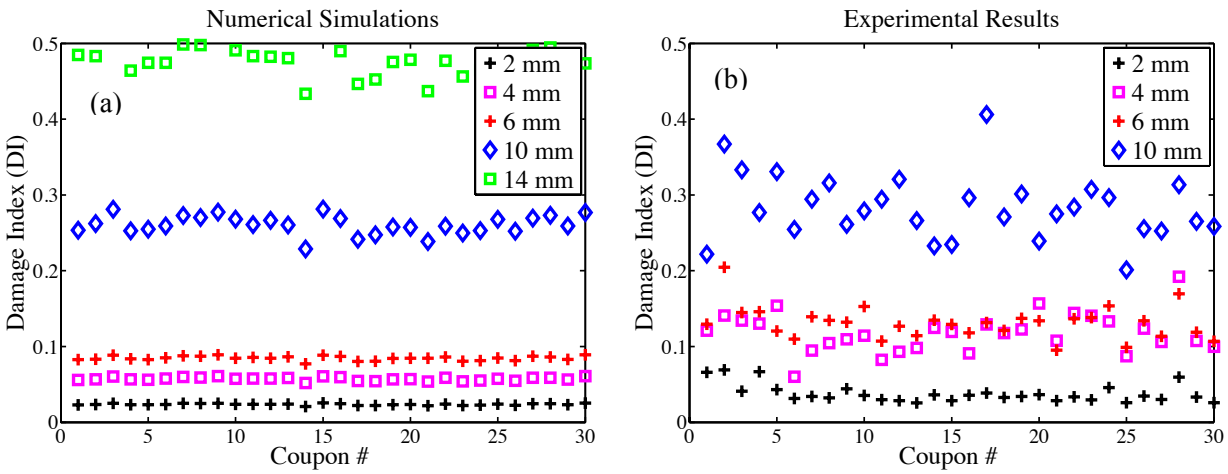

Figure 16: Effect of variation in damage size on the DI: (a) numerical simulations and (b) experimental results.

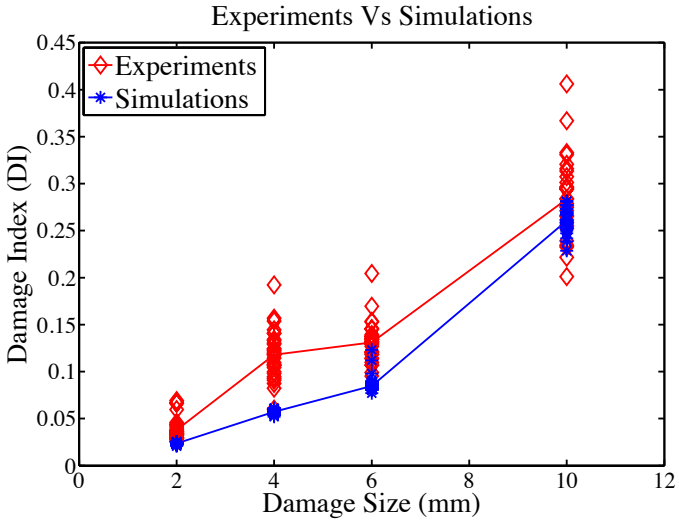

Figure 17: Numerical simulation versus experimental results: Effect of damage size on DI. The lines connect the mean values of the DIs for each damage size.

Variation in damage orientation. Figure 18 presents a real damage map observed from the thirty test coupons. Damages of 2 mm and 4 mm lengths were implemented via EDM machining. However, in order to increase the range of the uncertainties in this case, the 6 mm and 10 mm notch lengths were created manually using a thin hand saw which resulted in a different damage orientations and larger damage index variation.

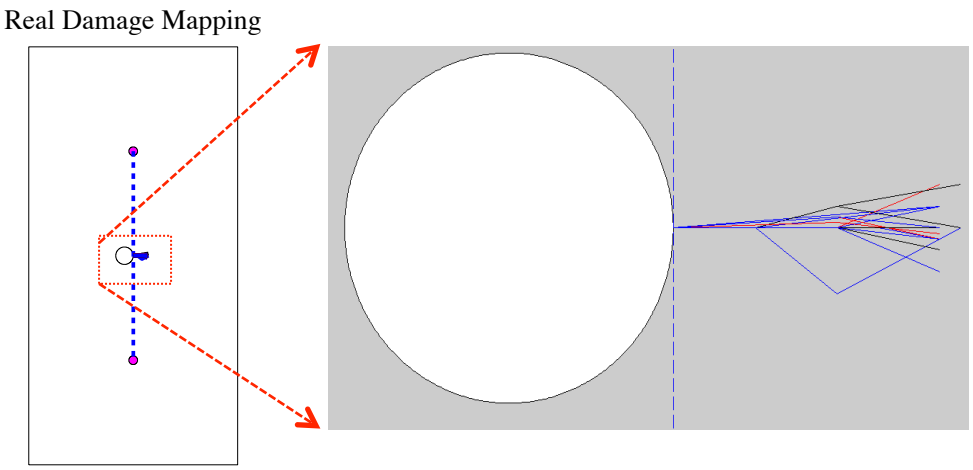

Figure 18: Mapping of the real damage (notches) for the thirty coupons.

Table 9: Summary of the parametric study: damage detection sensitivity characterization.

Property	**Property variation (%)**	**DI variation (%)**
Adhesive mechanical properties	2	0.58
PZT mechanical properties	5	0.55
PZT capacitance	20	
PZT electromechanical coefficients	20	
Structural properties	2	0.12
Sensor location	(±1.57*r, ±1.57*r)	10.84
Adhesive thickness	50	1.18

Where r- is the radius of PZT disc.

Discussion and Concluding Remarks

In this paper, the damage detection sensitivity characterization of an active-sensing acousto-ultrasound-based SHM method with respect to variations in the material properties, sensor installation, and damage propagation was investigated. The identification of the critical parameters that have a significant impact on the damage detection sensitivity was achieved via numerical simulations based on a Spectral Element Model-based analysis, analytical investigation, and experimental results obtained from multiple experiments on thirty aluminum coupons outfitted with a pair of PZT-based piezoelectric sensors/actuators. The results of this study indicated that the uncertainty in the sensor-actuator installation and the damage propagation path have a major impact on the sensing signals and the damage index calculation.

The main conclusions from this work are that the sensor locations with respect to the damage location and the way notch or cracks propagate are the two critical parameters that influence the damage index, if the environmental, ageing and boundary conditions remain constant. In that

respect, if the sensor-actuator location uncertainty can be minimized via accurate installation processes, then the damage growth exhibits a similar pattern from one coupon to another, and the damage index versus damage location behavior may be preserved for identical structures. Therefore, for a hotspot monitoring application (where the approximate damage location and orientation are known), testing of multiple coupons may not be necessary for traditional POD-based analysis under the assumption of accurate sensor installation, appropriate compensation of the environmental and boundary conditions effects, and compensation of aging effects. Numerical simulations through calibrated numerical models will help to minimize the number of components required for estimating the POD for SHM systems.

In order to develop an accurate and robust SHM system reliability quantification approach several fundamental multi-disciplinary techniques need to be further developed or extended in future research efforts and then combined in a unified framework. The developments required the most are related to the different challenges regarding accurate simulations under uncertainties and varying environmental/operating conditions, as different material models, reliable damage modeling, appropriate model calibration strategies, and uncertainty modeling and propagation techniques are required.

The concluding remarks of the study may be summarized as follows:

- The study shows that the sensor/actuator location and the damage growth orientation from specimen to specimen are the two major factors affecting the variation of the damage index for SHM under the same environmental and boundary conditions.
- The traditional POD-based method for NDE reliability quantification as presented in [13] may not be directly applicable for the case of SHM systems. However, improved methods based on sophisticated statistical models and appropriate methods may be able to tackle the various data structures observed in practice.
- Although duplicated coupon tests may provide adequate NDE quantification results, this practice may not be the optimal approach for quantifying SHM systems due to the inherent differences between NDE and SHM techniques. Accurate computational tools capable of effectively accounting for the major sources of uncertainty in SHM systems in combination with limited coupon tests may lead to less time consuming, less costly, and improved system reliability quantification results.
- More research work is needed with respect to (i) the definition of appropriate experimental procedures, (ii) accurate computational modeling techniques capable of accounting for operational and environmental uncertainty, and (iii) statistical methods and corresponding model building techniques for SHM reliability quantification.

Acknowledgment

The authors wish to thank the anonymous referees who provided constructive comments that helped in further improving the manuscript.

Funding

This research received no specific grant from any funding agency in the public, commercial, or not-for-profit sectors.

Bibliography

1. Ihn JB, Chang FK. Detection and Monitoring of Hidden Fatigue Crack Growth Using a Built-in Piezoelectric Sensor/Actuator Network, Part I: Diagnostics. Smart Materials and Structures. 2004; 13: p. 609-620.
2. Ihn JB, Chang FK. Detection and Monitoring of Hidden Fatigue Crack Growth Using a Built-in Piezoelectric Sensor/Actuator Network, Part II: Validation through Riveted Joints and Repair Patches. Smart Materials and Structures. 2004; 13: p. 621-630.
3. Lonkar K, Chang FK. Modeling of piezo-induced ultrasonic wave propagation in composite structures using layered solid spectral element. Structural Health Monitoring. 2014; 13: p. 50-67.
4. Broda D, Staszewski WJ, Martowicz A, Uhl T, V. SV. Modelling of nonlinear crack–wave interactions for damage detection based on ultrasound - A review. Journal of Sound and Vibration. 2014; 333(4): p. 1097-1118.
5. Croxford AJ, Wilcox PD, Drinkwater BW, Konstantinidis G. Strategies for guided-wave structural health monitoring. Proceedings of the Royal Society A. 2007; 463: p. 2961-2981.
6. Sharif-Khodaei Z, Aliabadi MH. Assessment of delay-and-sum algorithms for damage detection in aluminium and composite plates. Smart Materials and Structures. 2014; 23: p. 075007.
7. Flynn EB, Todd MD, Croxford AJ, Drinkwater BW, Wilcox PD. Enhanced detection through low-order stochastic modeling for guided-wave structural health monitoring. Structural Health Monitoring. 2011; 11(2): p. 149-160.
8. Sohn H, Lee SJ. Lamb wave tuning curve calibration for surface-bonded piezoelectric transducers. Smart Materials and Structures. 2010; 19: p. 015007.
9. Farrar CR, Worden K. An introduction to Structural Health Monitoring. The Royal Society – Philosophical Transactions: Mathematical, Physical and Engineering Sciences. 2007; 365: p. 303-315.
10. Giurgiutiu V, Soutis C. Guided wave methods for structural health monitoring. In Encyclopedia of Aerospace Engineering.: John Wiley & Sons, Ltd.; 2010.
11. Rummel WD. Recommended practice for demonstration of nondestructive (NDE) reliability on aircraft production parts. Materials Evolution. 1982; 40: p. 922-932.
12. Birks AC, Green P, McIntire P. Nondestructive testing handbook - Ultrasonic testing : Americal Society of Nondestructive Testing; 1991.
13. MIL-HDBK-1823. Nondestructive evaluation system reliability assessment. 1999: U.S. Department of Defense.
14. Matzkanin G, Yolken H. Probability of detection (POD) for Nondestructive Evaluation (NDE). Austin: Texas Research Institute; 2001.

15. Wall M, Burch SF, Lilley J. Review of models and simulators for NDT reliability (POD). Insight - Non-Destructive Testing and Condition Monitoring. 2009; 51(11): p. 612-619.
16. Roy S, Lonkar K, Janapati V, Chang FK. A novel physics-based temperature compensation model for structural health monitoring using ultrasonic guided waves. Structural Health Monitoring. 2014; 13(3): p. 321-342.
17. Chang FK, Larrosa C, Janapti V, Roy S, Lonkar K. A Robust Health Management System for Composite Airframe Structures. NRA Final Report to National Aeronautics and Space Administration (NASA). Stanford University, Department of Aeronautics and Astronautics; 2011.
18. Larrosa C, Lonkar K, Shankar S, Chang FK. Damage Classification in Composite Laminates; matrix Micro-Cracking and Delamination. In the 8th International Workshop on Structural Health Monitoring; 2011; Stanford,CA. p. 191-199.
19. Larrosa C, Chang FK. Real Time In-Situ Damage Classification, Quantification and Diagnosis for Composite Structures. In The 19th International Congress on Sound and Vibration; 2012; Vilnius, Lithuania.
20. Lonkar K, Janapati V, Roy S, Chang FK. A Model-assisted Integrated Diagnostics for Structural Health Monitoring. In AIAA Structures, Structural Dynamics and Materials; 2012; Hawaii.
21. Ihn JB, Chang FK. Pitch-catch Active Sensing Methods in Structural Health Monitoring for Aircraft Structures. Structural Health Monitoring: An International Journal. 2008; 7(1): p. 5-19.
22. Larrosa C, Janapati V, Roy S, Chang FK. In-situ Damage Assessment of Composite laminates Via Active Sensor Networks. In the Aircraft Airworthiness and Sustainment Conference; 2011a; San Diego, Ca.
23. Roy S, Chang FK, Lee SJ, Pollock P, V. J. A novel machine-learning approach for structural state identification using ultrasonic guided waves. In Proceedings of 11th International Conference on Structural Safety and Reliability; 2013; New York, USA.
24. Lu J, Lee SJ, Michaels JE, Michaels TE. On the optimization of temperature compensation for guided wave structural health monitoring. Review in Progress in Quantitative Nondestructuve Evaluation. 2010; 29.
25. Roy S, Ladpli P, Lonkar K, Chang FK. Structural damage detection using ultrasonic guided waves under varying ambient temperature and loading environments. In 9th IWSHM; 2013; Stanford.
26. Kopsaftopoulos FP, Fassois SD. A functional model based statistical time series method for vibration based damage detection, localization, and magnitude estimation. Mechanical Systems and Signal Processing. 2013; 39(1-2): p. 143-161.
27. Kopsaftopoulos FP, Fassois SD. A vibration model residual based sequential probability ratio test framework for structural health monitoring. Structural Health Monitoring. 2015; 14(4): p. 359-381.
28. Kopsaftopoulos FP, Fassois SD. Vibration based health monitoring for a lightweight truss structure: experimental assessment of several statistical time series methods. Mechanical Systems and Signal Processing. 2010; 24: p. 1977-1997.
29. Fassois SD, Kopsaftopoulos FP. Statistical Time Series Methods for Vibration Based Structural Health Monitoring. In Guemes A, Ostachowicz W, editors. New Trends in Structural Health Monitoring.:

Springer; 2013. p. 209-264.

30. Worden K, Manson G. The application of machine learning to structural health monitoring. Philosophical Transactions of the Royal Society A. 2007; 365: p. 515-537.
31. Oh CK, H. S. Damage diagnosis under environmental and operational variations using unsupervised support vector machines. Journal of Sound and Vibration. 2009; 328: p. 224-239.
32. Sohn H, Farrar CR. Damage diagnosis using time series analysis of vibration signals. Smart Materials and Structures. 2001; 10: p. 446-451.
33. Giurgiutiu V. Development and testing of high-temperature piezoelectric wafer active sensors for extreme environments. Structural Health Monitoring. 2010; 9: p. 513-525.
34. Salowitz N, Guo Z, Kim SJ, Li YH, Lanzara G, Chang FK. Microfabricated Expandable Sensor Networks for Intelligent Sensing Materials. IEEE Sensors Journal. 2014.
35. Salowitz N, Guo Z, Kim SJ, Li YH, Lanzara G, Chang FK. Screen Printed Piezoceramic Actuators/Sensors Microfabricated on Organic Films and Stretchable Networks. In Structural Health Monitoring 2013 - A Roadmap to Intelligent Structures; 2013; Stanford, CA. p. 1543-1550.
36. Rytter A. Vibration based inspection of civil engineering structures. PhD Thesis. Aalborg: Aalborg University, Department of Building Technology and Structural Engineering; 1993.
37. Mueller I, Janapati V, Banerjee S, Lonkar K, Roy S, Chang FK. On the performance quantification of active sensing SHM systems using model-assisted POD methods. In Chang FK, editor. Proceedings of the 8th International Workshop on Structural Health Monitoring; 2011; Stanford: DesTech Publications, Inc. p. 2417-2428.
38. SAE International. Aerospace Recommened Practice ARP6461: Guidelines for Implementation of Structural Health Monitoring on Fixed Wing Aircraft. September 2013.
39. Schubert-Kabban AC, Derriso MM. Certification in structural health monitoring systems. In Chang FK, editor. Proceedings of the 8th International Workshop on Structural Health Monitoring; 2011; Stanford: DesTech Publications, Inc. p. 2429-2436.
40. Lindgren EA, Buynak CF. The Need and Requirements for Validating Damage Detection Capability. In Chang FK, editor. Proceedings of the 8th International Workshop on Structural Health Monitoring; 2011; Stanford: DEStech Publications, Inc. p. 2444-2451.
41. Aldrin JC, Medina EA, Lindgren EA, Buynak CF, Knopp JS. Protocol for Reliability Assessment of Structural Health Monitoring Systems Incorporating Model-assisted Probability of Detection (MAPOD) Approach. In Chang FK, editor. Proceedings of the 8th International Workshop on Structural Health Monitoring; 2011; Stanford: DEStech Publications, Inc. p. 2452-2459.
42. Medina EA, Aldrin JC, Santiago J, Lindgren EA, Buynak CF, S. KJ. Demonstration of Model Assisted Reliability Assessment Protocol on a Proposal Low Frequqncy Vibration Based Damage Sensing Case. In Chang FK, editor. Proceedings of the 8th International Workshop on Structural Health Monitoring; 2011; Stanford: DEStech Publications, Inc. p. 2460-2467.
43. Le DD, Ghoshal A, Cuevas E. Condition-based Maintenance Plus and Maintenance Credit Validation. In Chang FK, editor. Proceedings of the 8th International Workshop on Structural Health Monitoring; 2011; Stanford: DEStech Publications, Inc. p. 2485-2492.

44. Gagar D, Irving P, Jennions I, Foote P, Read I, McFeat J. Development of Probability of Detection Data for Structural Health Monitoring Damage Detection Techniques Based on Acoustic Emission. In Chang FK, editor. Proceedings of the 8th International Workshop on Structural Health Monitoring; 2011; Stanford: DEStech Publications, Inc. p. 1391-1398.
45. Brausch J, Steffes G. Demonstration, Qualification, and Airworthiness Certification of Structural Damage Sensing (SDS) Systems for Air Force Application. No. AFRL-RX-WP-TM-2013-0062. Air Force Research Lab Wright-Patterson AFB OH Materials And Manufacturing Directorate, 2013.
46. Park S, Park G, Yun C-B, Farrar CR. Sensor self-diagnosis using a modified impedance model for active sensing-based structural health monitoring. Structural Health Monitoring. 2009; 8(1): p. 71-82.
47. Mulligan KR, Quaegebeur N, Masson P, Brault L-P, Yang C. Compensation of piezoceramic bonding layer degradation for structural health monitoring. Structural Health Monitoring. 2014; 13(1): p. 68-81.
48. Annis C, Aldrin JC, Sabbagh HA. What is Missing in Nondestructive Testing Capability Evaluation?. Materials Evaluation, 2015. 73(1): p. 44-54.
49. Schubert Kabban C, Greenwell B, DeSimio M, Derriso M. The probability of detection for structural health monitoring systems: Repeated measures data. Structural Health Monitoring. 2015; 14(3): p. 252-264.
50. Hosten B, Moreau L, Castaings M. Reflection and transmission coefficients for guided waves reflected by defects in viscoeleastic material plates. Journal of Acoustical Society of America. 2007; 121(6): p. 3409-3417.
51. Ostachowicz W, Kudela P. Wave propagation numerical models in damage detection based on the time domain spectral element method. IOP Conference Series: Material Science Engineering. 2010; 10: p. 012068.
52. Ha S. Modeling Lamb Wave Propagation Induced by Adhesively Bonded PZTs on Thin Plates Stanford: Ph.D. Dissertation, Stanford Univ., CA; 2009.
53. Patera AT. A Spectral Element Method for Fluid Dynamics: Laminar Flow in a Channel Expansion. Journal of Computational Physics. 1984; 54: p. 468-488.
54. Lonkar K. Modeling of Piezo-Induced Ultrasonic Wave Propagation for Structural Health Monitoring Stanford: PhD Thesis; 2013.
55. Lonkar K, Chang FK. Development of SEM-based PESEA Code for Modeling PZT Induced Acousto-Ultrasonic Waves Propagating in Metallic & Composite Structures. In the 8th International Workshop on Structural Health Monitoring; 2011; Stanford: DEStech Publications. p. 2512-2520.
56. Lanza Di Scalea F, Salamone S. Temperature Effects in Ultrasonic Lamb Wave Structural Health Monitoring Systems. Journal of Acoustic Society of America. 2008; 124(1): p. 161-174.